

## Article

# Effects of B and Ce Grain Boundary Segregation on Precipitates in Super Austenitic Stainless Steel

Song Yang <sup>1</sup>, Jinyao Ma <sup>1,2</sup>, Chao Chen <sup>1</sup> , Caili Zhang <sup>1</sup>, Junyu Ren <sup>1</sup>, Zhouhua Jiang <sup>3</sup>, Guangwei Fan <sup>2</sup> and Peide Han <sup>1,\*</sup>

<sup>1</sup> College of Materials Science and Engineering, Taiyuan University of Technology, Taiyuan 030024, China

<sup>2</sup> Technical Center of Taiyuan Iron and Steel (Group) Company Ltd., Taiyuan 030024, China

<sup>3</sup> School of Metallurgy, Northeastern University, Shenyang 110167, China

\* Correspondence: hanpeide@tyut.edu.cn

**Abstract:** In order to reduce the segregation of Cr and Mo and inhibit the precipitates, we added a small amount of B and Ce to traditional S31254 steel. Using an air-cooling and low-temperature diffusion treatment, the purpose was to control B and Ce at the grain boundary. The heat-treatment process could prompt co-segregation of B, precipitate-forming elements, and Ce at the grain boundary at 950 °C. After aging at 950 °C for different amounts of time, the diffusion treatment had an obvious inhibitory effect on the precipitates that caused them to become discontinuous, fine, and serrated. The B-containing serrated precipitates were only rich in Mo, while Cr was homogeneously distributed in the probed volume. A uniform distribution of Cr reduced the Cr-depleted zone in the area adjacent to the phase interface. Ce was observed to be segregated at the grain boundary. This showed that Ce could inhibit the formation of precipitates at the grain boundary. The serrated precipitates had an obvious resistance to intergranular corrosion.

**Keywords:** super austenitic stainless steel; precipitates; boron; diffusion treatment; corrosion resistance



**Citation:** Yang, S.; Ma, J.; Chen, C.; Zhang, C.; Ren, J.; Jiang, Z.; Fan, G.; Han, P. Effects of B and Ce Grain Boundary Segregation on Precipitates in Super Austenitic Stainless Steel. *Metals* **2023**, *13*, 326. <https://doi.org/10.3390/met13020326>

Academic Editor: Pavel Lejček

Received: 13 January 2023

Revised: 1 February 2023

Accepted: 3 February 2023

Published: 6 February 2023



**Copyright:** © 2023 by the authors. Licensee MDPI, Basel, Switzerland. This article is an open access article distributed under the terms and conditions of the Creative Commons Attribution (CC BY) license (<https://creativecommons.org/licenses/by/4.0/>).

## 1. Introduction

Super austenitic stainless steel (SASS) is an important developmental direction of high-performance stainless steels. Since the beginning of the 20th century, a number of SASSs have been developed to satisfy the demands for high corrosion resistance and long-life materials [1–3]. These steels have excellent pitting corrosion resistance due to their high Cr, Mo, and N contents [4,5]. They can partly replace nickel-based alloys [6]. However, due to the addition of excessive amounts of Cr and Mo, S31254 SASSs are prone to Mo segregation during hot rolling, which forms  $\sigma$ , thereby introducing serious problems in hot rolling cracking and corrosion resistance [7–9]. Therefore, it is very necessary to explore methods to reduce Mo segregation and  $\sigma$  phase precipitation to solve the hot working and corrosion resistance problems of S31254.

Alloying is often used to improve the properties and microstructure of a material. For example, adding Ni, N, or Mn to austenitic stainless steel can play a positive role in stabilizing the austenite matrix and inhibit the precipitation of  $\sigma$  [1,10,11]. In recent years, many studies have been conducted on the inhibition of precipitates by using microalloying. It is known that the addition of a small amount of boron (B) to austenitic alloys significantly increases their hardenability in continuous cooling from austenite. It is mainly understood that the segregation of boron at the austenite grain boundary lowers the grain boundary energy, thereby resulting in the inhibition of ferrite and bainite transformation. The effect can be obtained using only a very small amount of boron (on the order of ppm) to provide significant impacts on the production of alloys. However, it is not easy to control the effect of B in an industrial production process because the state of the B atoms in the steel significantly influences the effect on hardenability [12,13]. At the same time, the addition

of B can inhibit the formation of precipitates and improve the corrosion resistance [14,15]. Zhang Y. et al. improved the corrosion resistance of S31254 via B-induced nucleation of the Laves phase. The results showed that B alloying could significantly inhibit the  $\sigma$  phase formation and induce nucleation of the Laves phase. Furthermore, the Laves phase that contained B decreased the Cr-depleted zones near the grain boundaries and reduced the interface potential difference, which could enhance the intergranular corrosion resistance [16]. Yu et al. studied the effect of B on the thermal ductility of S32654. During thermal deformation, B could improve the hot ductility of S32654 and inhibit the  $\sigma$  phase nucleation. The segregation of B inhibited the segregation of Mo at the GB and enhanced the cohesion of the GB [17]. Previous studies showed that B was more inclined to exist at GBs and had the effect of inhibiting precipitation. These studies confirmed the assumption that the B atom is easy to segregate at the GB. At the same time, the addition of Ce to some types of steel can also inhibit precipitation. Wang et al. added Ce to duplex stainless steel, after which the stability of hot working was improved, the deformation resistance was decreased, the temperature range of hot working was widened, and the hot ductility was improved. Ce was segregated at the GB, and the inclusions were modified. By controlling the reasonable content of Ce in the steel, the molten steel could be purified [18]. At the same time, there are precedents for adding Ce to duplex stainless steel [19] and S32654 [20].

To clarify the state and distribution of B, the direct observation of B segregation at prior austenite grain boundaries was performed using the alpha-ray track etching method (ATE) and secondary ion mass spectroscopy (SIMS). These two analysis methods are very sensitive to B segregation; however, quantitative analysis of the amount was difficult. B segregation can be controlled either by equilibrium segregation (ES) or non-equilibrium segregation mechanisms (NES). On the one hand, the driving force for ES is a decrease in the system total energy caused by solute atom migration from the matrix to the structural defects. For the same solute concentration in a given solid solution, the ES magnitude decreases with an increasing temperature, which will be discussed later. On the other hand, NES results from the formation of solute–vacancy complexes within the matrix [21,22].

The effect of B on precipitates can be mainly determined by the non-equilibrium segregation of B to GBs during cooling after austenitization. Non-equilibrium grain boundary segregation of B during cooling from high temperatures results from diffusion of vacancy–boron complexes toward vacancy sinks and is very sensitive to the temperature difference. The boron concentration profile changes with the cooling rate from the solid solution temperature. The concentration of B at grain boundaries was maximized at an appropriate cooling rate in low-alloy steel [23]. At the same time, previous studies showed that adding a trace amount of Ce to S31254 could reduce the total amount of  $\sigma$  in S31254; in particular, the addition of Ce significantly inhibited  $\sigma$  formation, and slow cooling was conducive to the diffusion of Ce to the GB [24]. These phenomena were attributed by some authors to the non-equilibrium segregation of boron to austenite grain boundaries. It is widely accepted that B or Ce segregation at prior austenite grain boundaries during cooling is controlled by a non-equilibrium mechanism. Therefore, B and Ce can be better diffused to the grain boundary by changing the cooling method. Simultaneously, intragranular B is in a supersaturated state after dissolving, and B can be further aggregated at the grain boundary through a lower-temperature heat treatment.

In addition, the effects of the combined addition of B and Ce to S31254 have not been previously reported. To clarify the distribution of B and Ce, air cooling and low-temperature diffusion were used to further segregate B and Ce at the grain boundary, and the influence of B and Ce at the grain boundary on the precipitates during aging and the corresponding corrosion resistance were further studied.

## 2. Materials and Methods

### 2.1. Materials

The material used in this investigation was a new type of super austenitic stainless steel (S32654) manufactured by Northeastern University, Shenyang, China. The steel was

smelted in a vacuum induction melting furnace followed by an electroslag remelting furnace to obtain lower sulfur and phosphorus contents and suppress segregation. The ingots were cast into 120 mm × 100 mm × 500 mm ingots and taken out of the mold after being air-cooled. The ingots were kept at 1200 °C for 10 h in a resistance heating furnace, cooled to room temperature by air, and then heated to 1250 °C and kept for 30 min in the furnace. Then, a steel plate with a thickness of 28 mm was rolled on the Φ550 mm hot rolling mill and hot forged and hot rolled between 1150 and 1200 °C. The main chemical components used are shown in Table 1. The plate was cut into 15 mm × 15 mm × 2 mm sections using an electric-spark numerical-control wire-cutting machine.

**Table 1.** Chemical composition of S31254 used in the experiment (wt %).

Sample	Fe	C	Si	Mn	P	S	Cr	Ni	Mo	Cu	N	B	Ce
S31254–BCe	Bal.	0.017	0.16	1.68	0.007	0.002	19.99	17.76	5.85	0.96	0.21	0.004	0.004

## 2.2. Heat-Treatment Process

Figure 1 shows the curve of the heat-treatment process. First, in the conventional heat-treatment process (hereinafter referred to as SW), we kept the S31254–BCe at 1200 °C for 30 min and then quenched it in water. In the second heat-treatment process (hereinafter referred to as AD), we kept the S31254–BCe sample at 1200 °C for 30 min and then lowered the temperature to 1100 °C within 15 min in the furnace. The cooling method was air cooling, a diffusion treatment at 300 °C for 40 min, and then air cooling again. Then, in order to test the inhibition effect of the AD treatment on the precipitates, the samples of the SW and AD treatments were aged at a precipitation-sensitive temperature (950 °C) for 15 min, 1.5 h, 3 h, and 6 h respectively.

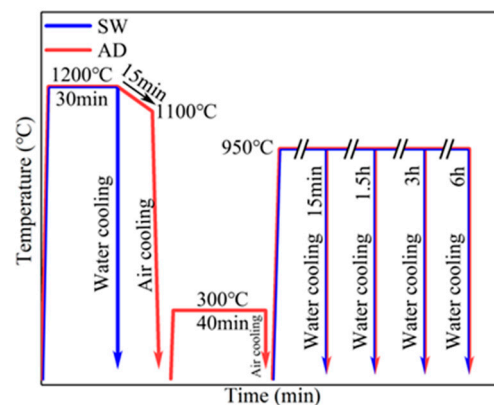


**Figure 1.** Schematic diagram of heat-treatment process.

## 2.3. Microstructure Characterization

After heat treatment, the samples were inlaid with epoxy resin at room temperature; water polished with 120#, 400#, 1000#, and 3000# sandpaper; then polished with 1.5 μm diamond polishing paste until there were no scratches on the surface of the samples; then cleaned with ethanol and distilled water using an ultrasonic bath. After the surface of a sample was corroded with aqua regia, the microstructure of the sample was photographed using a JEOL SM-7900F thermal field emission scanning electron microscope (SEM), and then we analyzed the composition of the precipitates in local areas with an energy-dispersive spectrometer (EDS). We further analyzed the distribution of B, Ce, and the element content of the precipitates using a JEM-F200 scanning transmission electron microscopy (STEM).

#### 2.4. Corrosion-Resistance Test

A CS310H electrochemical workstation was used for potentiodynamic polarization scanning and electrochemical impedance spectroscopy (EIS). The electrolyte was green-death solution (4 g  $\text{CuCl}_2$ , 4 g  $\text{FeCl}_3$ , 24.76 mL concentrated  $\text{H}_2\text{SO}_4$ , 4.072 mL HCl, and 341.6 mL water) [25]. Electrochemical tests were repeated to avoid errors. The electrolytic cell used in the experiment was a double-layer flat electrolytic cell, and the experiment was a three-electrode system. The working electrode (WE) was connected to the sample to be tested. A saturated calomel electrode (SCE) was selected as the reference electrode, and a platinum electrode (PE) was used as the auxiliary electrode. The contact area between a sample and the electrolyte was  $10\text{ cm} \times 10\text{ cm}$ . The processing and analysis of the test data was conducted using the electrochemical analysis software system Corrtest 5.0.

In order to further explore the corrosion resistance, S31254-BCe steel subjected to different heat-treatment processes was immersed in boiling  $\text{H}_2\text{SO}_4\text{-Fe}_2(\text{SO}_4)_3$  (Practice B of ASTM-A262) [26]. The specific method for this experiment was as follows: first, we added 200 mL of distilled water to a 500 mL round bottom flask and then slowly added 118.0 mL of analytical-grade concentrated  $\text{H}_2\text{SO}_4$  (the concentration had to be between 95.0 and 98.0%) to avoid boiling due to overheating. Then, we weighed 12.5 g of iron sulfate (containing about 75%  $\text{Fe}_2(\text{SO}_4)_3$ ) and added it to the above  $\text{H}_2\text{SO}_4$  solution. We then connected the circulating condenser to the bottle mouth of the flask, lubricated the frosted glass joint with silicone grease, connected the circulating condenser to drain the water, and finally boiled the solution until all of the iron sulfate was dissolved. We then immersed the polished sample in a boiling  $\text{H}_2\text{SO}_4\text{-Fe}_2(\text{SO}_4)_3$  solution for 24 h and then removed the sample for cleaning and drying.

### 3. Results

#### 3.1. Precipitation Behavior

Figure 2a–h show the microstructures of samples treated using SW or AD. The samples were aged at  $950\text{ }^\circ\text{C}$  for 15 min, 1.5 h, 3 h, or 6 h. Figure 2a,e show the microscopic morphology of the samples aged at  $950\text{ }^\circ\text{C}$  for 15 min. It can be seen that there was no precipitation at the GB. Due to the addition of B and Ce, the precipitates were obviously inhibited. As the aging time was increased to 1.5 h (Figure 2b,f), the precipitates were intermittently distributed at the GB of the samples treated using SW. Previous research by our group showed that the precipitates appeared at the GB after 15 min of aging in S31254. The precipitates were connected in a network along the GB after 1.5 h of aging [27]. The addition of B and Ce initially inhibited the precipitates. After AD treatment, the number of precipitates decreased significantly and the size became smaller under the same aging time. After aging at  $950\text{ }^\circ\text{C}$  for 3 h, the precipitates of the SW-treated samples separated out along the GB and began to form a network. However, the precipitates of the samples treated using AD were significantly fewer and were generally serrated precipitates, and the distribution of the precipitates was more discontinuous. This proved that the AD treatment could still inhibit the precipitates when aged at  $950\text{ }^\circ\text{C}$  for 3 h. After aging for 6 h, the precipitates formed in the SW treatment connected into a network along the GB. The precipitates formed in the AD treatment were intermittently distributed at the GBs but also tended to form a network. It can be seen that the AD treatment further inhibited the precipitates on the basis of adding B and Ce.

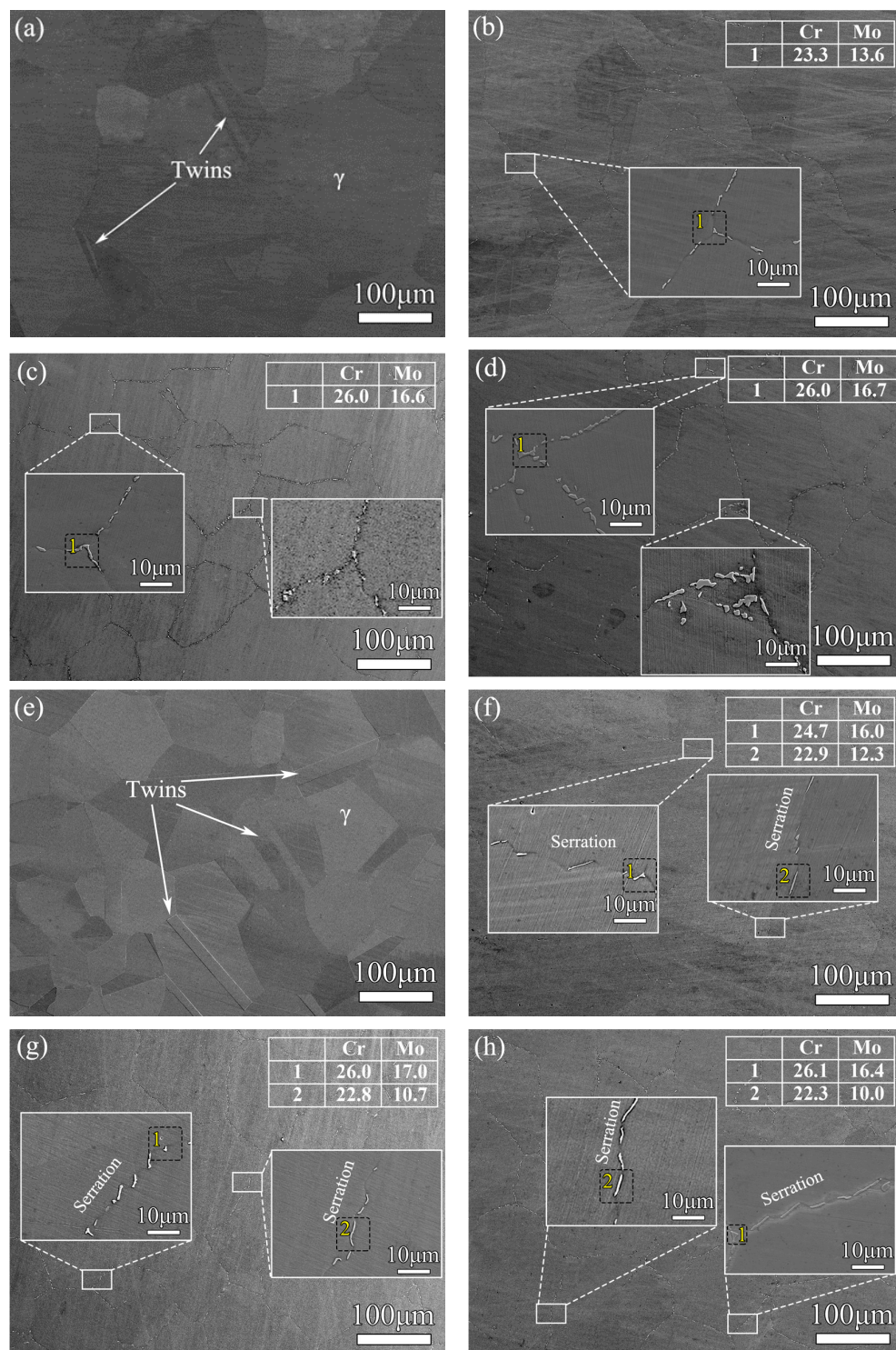


**Figure 2.** Microstructures at 950 °C at different aging times: (a) SW 15 min; (b) SW 1.5 h; (c) SW 3 h; (d) SW 6 h; (e) AD 15 min; (f) AD 1.5 h; (g) AD 3 h; (h) AD 6 h.

As shown in Figure 2, the precipitates were distributed at the straight GB at a greater proportion. Distinct from the SW treatment, serrated precipitates accounted for a greater proportion after AD treatment. In order to further analyze the changes in the elements in the precipitates, the SEM-EDS analysis method was used to measure the element distribution in the sample. EDS maps of the alloying elements (Fe, Cr, Mo, and B) were acquired to observe the elemental concentration of the precipitates. Figure 3a,b show the precipitates after SW treatment at an aging time of 1.5 h and 6 h, respectively. The precipitates were rich

in both Cr and Mo. Based on the analysis of the EDS point scanning data in shown Figure 2, the precipitates distributed at the straight GB were consistent with  $\sigma$  in S31254 steel due to its high Cr and Mo content [27]. Figure 3c shows the precipitates after AD treatment; the serrated precipitates were only rich in Mo. At the same time, obvious enrichment of B could be observed during precipitation. This could prove that the serrated precipitates contained B and Mo simultaneously and that the formation of the serrated precipitate was related to the element B and would affect the distribution of Cr. The substitutional solute Cr was homogeneously distributed throughout the entire detected volume. This phenomenon indicated that the addition of B may have effectively reduced the aggregation of Cr in the precipitates, thus affecting the corrosion resistance of the material. Next, the corrosion resistance was further analyzed. Ordinary S31254 SASSs separated out a large number of precipitates after aging at 950 °C for 6 h, which formed a continuous network distribution along the GB [27]. The addition of B and Ce could effectively inhibit the precipitates. In particular, serrated precipitates that contained B can make the precipitates finer and fewer.

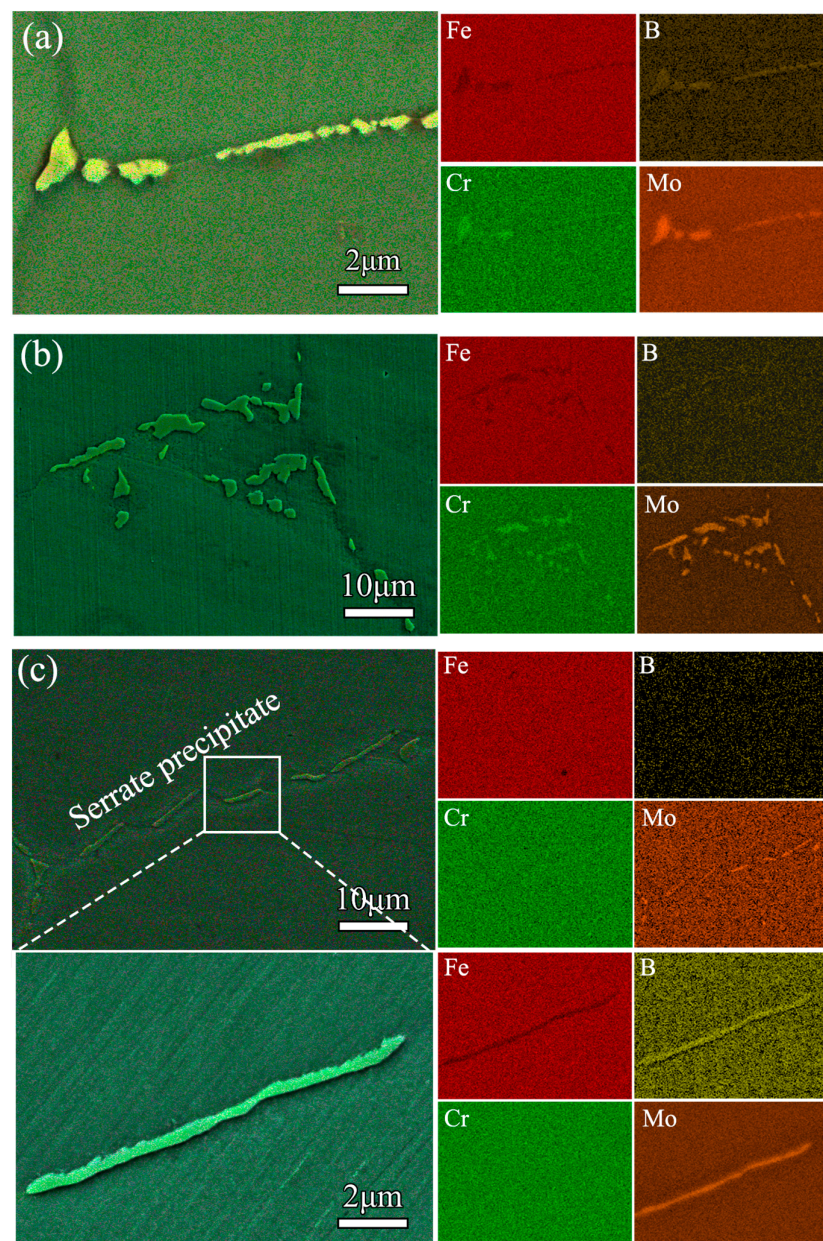


**Figure 3.** EDS spectrum of precipitates after aging at 950 °C: (a) SW sample aged for 1.5 h; (b) SW sample aged for 6 h; (c) AD sample aged for 6 h.

### 3.2. Corrosion Resistance

In order to explore the relationship between the precipitates and corrosion resistance, potentiodynamic polarization scanning and electrochemical impedance spectroscopy were carried out.

Figure 4 shows the potentiodynamic polarization curves of S31254–BCe samples aged for different amounts of time (15 min, 1 h, or 3 h) in green-death solution. The cathodic polarization curves showed similar trends; based on the polarization curves, the corrosion resistance of the sample aged for 15 min was the best. In particular, the corrosion resistance of AD samples was better than that of SW samples within 15 min aging. Their anode branches showed obvious self-passivation characteristics in the green-death solution environment. In order to describe the evolution of passivation performance in detail, the electrochemical parameters were calculated by fitting the polarization curve; the results are shown in Table 2. There were differences in the self-corrosion current density ( $i_{\text{corr}}$ ), self-corrosion potential ( $E_{\text{corr}}$ ), pitting current density ( $i_{\text{pit}}$ ), and pitting potential ( $E_{\text{pit}}$ ) between the samples treated using SW or AD.

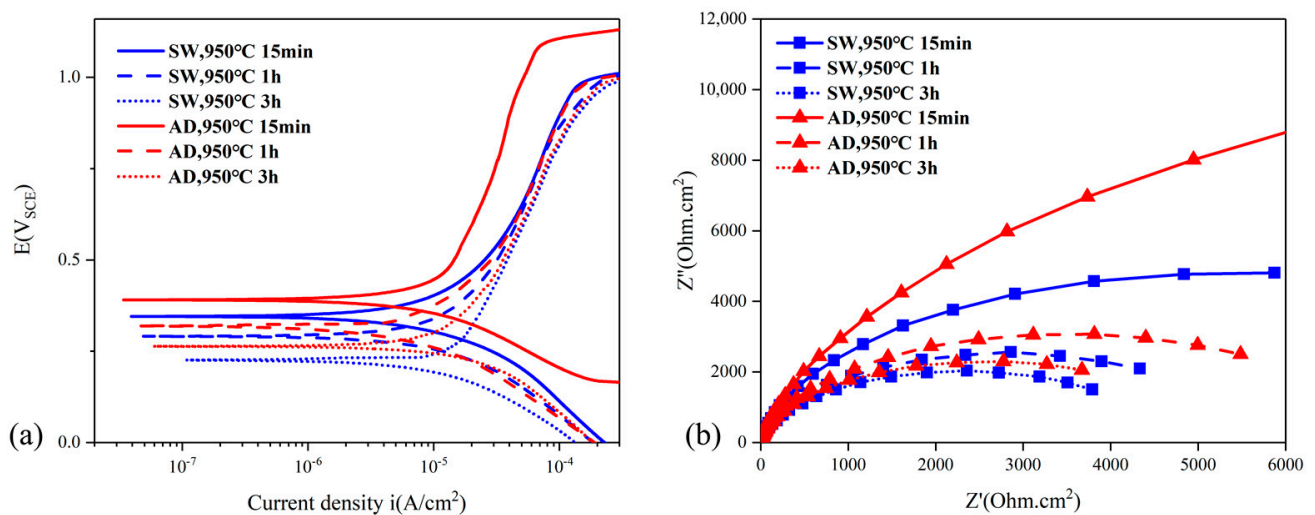


**Figure 4.** (a) Potentiodynamic polarization curves; (b) electrochemical impedance spectroscopy results.

**Table 2.** Main parameters of potentiodynamic polarization curves of S31254–BCe aged at different times using different heat-treatment processes.

Sample	Aging Time	$E_{\text{corr}}$ (V)	$I_{\text{corr}}$ ( $\text{A cm}^{-2}$ )	$E_{\text{pit}}$ (V)	$I_{\text{pit}}$ ( $\text{A cm}^{-2}$ )
S31254–BCe (SW)	15 min	0.347	$1.271 \times 10^{-5}$	0.981	$1.426 \times 10^{-4}$
	1 h	0.293	$1.725 \times 10^{-5}$	0.972	$1.828 \times 10^{-4}$
	3 h	0.224	$2.343 \times 10^{-5}$	0.959	$2.117 \times 10^{-4}$
S31254–BCe (AD)	15 min	0.391	$1.091 \times 10^{-5}$	1.091	$7.238 \times 10^{-5}$
	1 h	0.32	$1.482 \times 10^{-5}$	0.976	$1.504 \times 10^{-4}$
	3 h	0.267	$1.814 \times 10^{-5}$	0.965	$1.961 \times 10^{-4}$
S31254 without BCe [28]	Solution	0.162	$1.203 \times 10^{-6}$	0.957	$2.042 \times 10^{-5}$

Compared with S31254 without B and Ce [28], the addition of B and Ce improved the corrosion resistance, which was further improved by the AD treatment. In addition, with the extension of the aging time, the self-corrosion current density ( $i_{\text{corr}}$ ) of the samples gradually increased. The self-corrosion current density ( $i_{\text{corr}}$ ) of the SW samples increased from  $1.271 \times 10^{-5}$  to  $2.343 \times 10^{-5}$   $\text{A cm}^{-2}$ , while the self-corrosion current density ( $i_{\text{corr}}$ ) of the AD samples increased from  $1.091 \times 10^{-5}$  to  $1.814 \times 10^{-5}$   $\text{A cm}^{-2}$ , which showed

that with the extension of the aging time, the precipitates at the GB gradually increased, which had an adverse impact on the corrosion resistance. Moreover, under the same aging time, the self-corrosion potential ( $E_{\text{corr}}$ ) of the AD samples was higher than that of the SW samples, which indicated that the corrosion resistance of the material was significantly improved after the AD treatment. This phenomenon occurred because the number of precipitates at the GB decreased after the AD treatment. Then, in order to further analyze the characteristics of the passive film formed in the green-death solution, the samples were further tested using electrochemical impedance spectroscopy.

Figure 4b shows the EIS spectra of the samples. The Nyquist diagram (Figure 4b) showed similar data trends, which indicated that the electrode reaction mechanism was consistent and that there was a capacitance semicircle from the high-frequency region to the low-frequency region. The intermediate frequency phase angle was close to  $-90^\circ$ , which indicated that a stable passive film was formed. Under the same aging time, the capacitance semicircle radius of the samples treated using AD was larger than that treated using SW.

The surface morphologies of the S31254–BCe samples after electrochemical polarization were analyzed. Figure 5a,b show the samples aged at  $950^\circ\text{C}$  for 15 min after SW or AD treatment, respectively. After polarization, the surfaces of the samples were smooth, and there was no corroded GB. According to the microstructures of the samples with 15 min of aging shown in Figure 2, there were no precipitates at the GB. With the aging time extended to 3 h, the precipitates treated using SW tended to form a network at the GB (Figure 2). After polarization, the corrosion pits left after the precipitation phase fell off were wide and continuous. However, after polarization of the AD-treated samples, the proportion of serrated precipitates increased obviously, and the corrosion pits left after the serrated precipitates fell off were narrow and intermittent. Combined with the results shown in Figures 2 and 3, the precipitates treated using SW were rich in both Cr and Mo universally, and the precipitate interface was corroded after polarization, which indicated that there was a Cr-depleted zone around the precipitate interface and that the corrosion resistance would be affected adversely. The serrated precipitate was only rich in Mo, and Cr was homogeneously distributed in the probed volume. The phase interface was relatively complete after polarization, which indicated that there was no Cr-depleted zone around the phase interface. At the same time, the morphology results after polarization were consistent with the electrochemical curve results. The corrosion resistance of the serrated precipitates was better than that of the common precipitates at straight GBs.

Figure 6 shows sample surfaces after immersion in boiling  $\text{H}_2\text{SO}_4\text{-Fe}_2(\text{SO}_4)_3$  for 24 h. The corrosion morphology corresponding to this precipitate was the severely corroded periphery of the precipitate after SW treatment (Figure 6c). After AD treatment, the corrosion resistance at the phase interface was significantly improved, which indicated that the corrosion resistance of the serrated precipitates was obviously different from the precipitates at the straight GB. This meant that the precipitates at the straight GB were rich in both Cr and Mo, which led to a Cr-depleted zone around them. As shown in Figure 6a, a small number of intragranular corrosion pits also appeared after SW treatment, which should have been related to the intragranular precipitates. However, the number of intragranular corrosion pits was significantly reduced after the AD treatment, which indicated that the AD treatment also had a significant inhibitory effect on the intragranular precipitates.

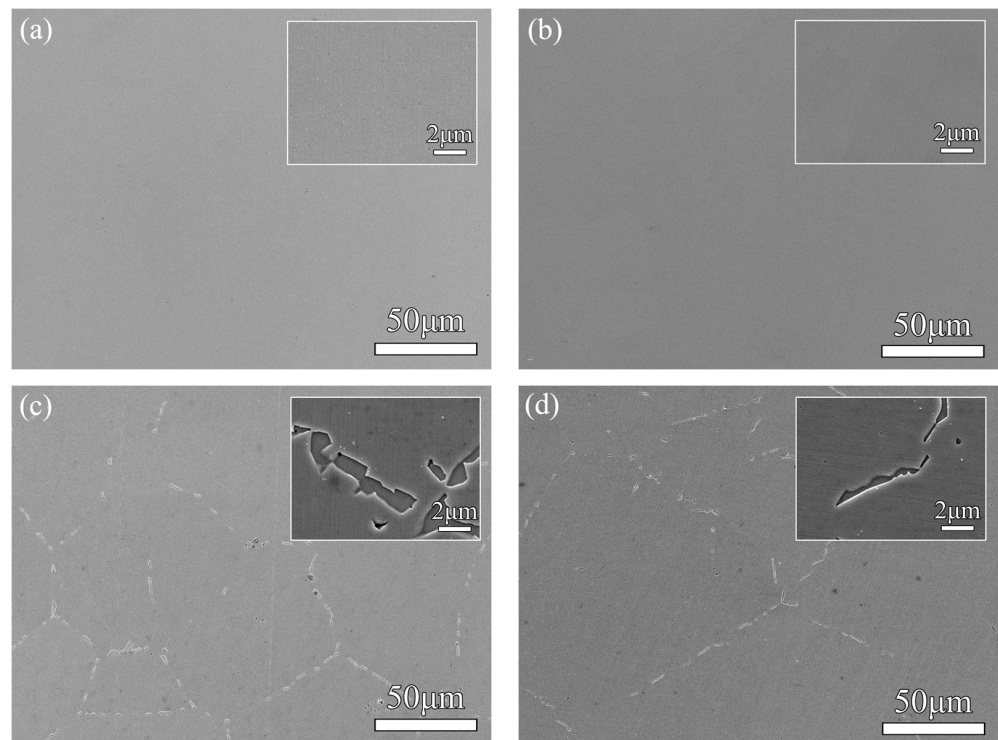


**Figure 5.** Surface morphology of samples after electrochemical test: (a) SW aged at 950 °C for 15 min; (b) AD aged at 950 °C for 15 min; (c) SW aged at 950 °C for 3 h; (d) AD aged at 950 °C for 3 h.

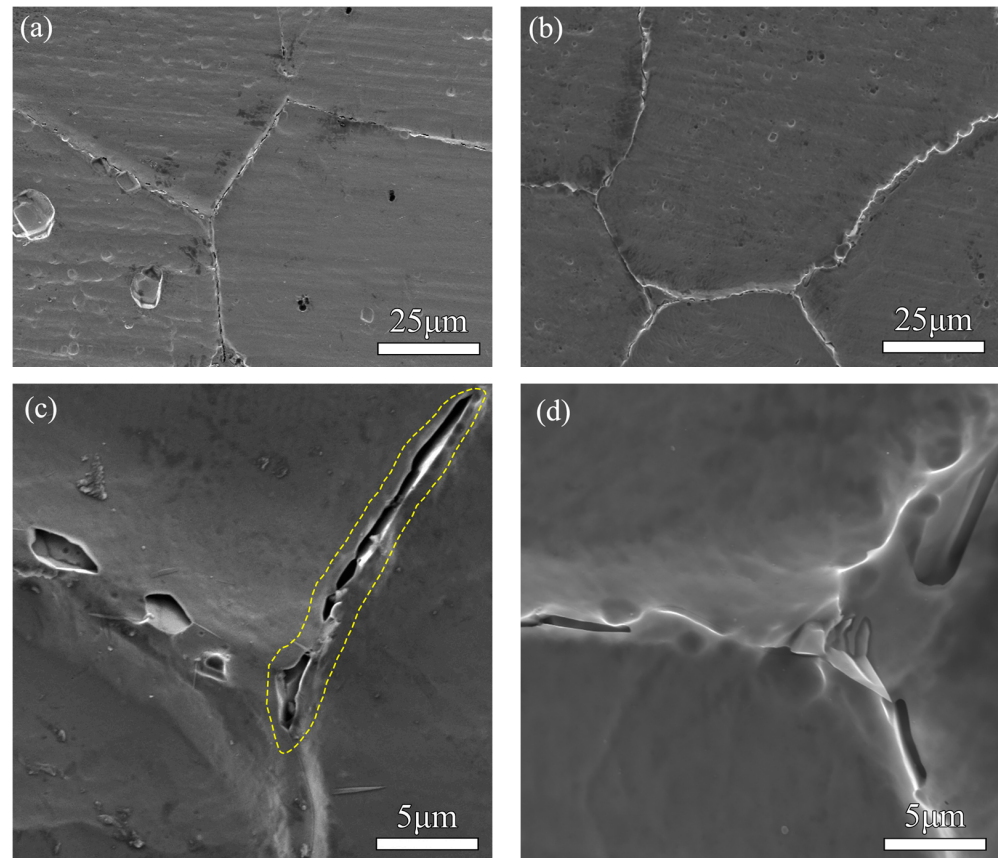


**Figure 6.** Microstructures of S31254–BCe samples aged for 3 h and soaked in boiling  $\text{H}_2\text{SO}_4\text{-Fe}_2(\text{SO}_4)_3$  for 24 h: (a,c) samples treated using SW; (b,d) samples treated using AD.

#### 4. Discussion

The solubility of B and Ce in  $\gamma$  is very limited. Depending on the thermal cycle (soaking temperature, cooling rate, and final cooling temperature), B and Ce segregation can be controlled either by equilibrium segregation or non-equilibrium segregation [21,22]. In order to distribute more B and Ce elements to the GBs, the cooling rate was changed. At the solid solution temperature, the supersaturated solid solution was often obtained due to the high cooling speed. Therefore, slow cooling was used to further distribute more B and Ce to GB. Slow cooling was conducive to the diffusion of Ce to GB, which was limited by the influence of precipitates at the range of precipitation-sensitive temperature, so the low-temperature diffusion at 300 °C was adopted. Through the heat treatment of slow cooling and low-temperature diffusion, B and Ce could be more diffused to the GB and play their roles in inhibiting precipitation [24]. According to the EDS of STEM, the enrichment of Ce at GB was observed in the sample after AD treatment. Although the addition of Ce was less, we determined that the content of Ce at the GB was higher than in the matrix. Position 3 contained Ce, and Ce mainly existed at the GBs. Cr and Mo at position 3, which was close to the matrix, were obviously diminished. This indicated that Ce at the GBs could inhibit the formation of precipitates and caused the precipitates to distribute intermittently. After the low-temperature diffusion at 300 °C, the GBs showed an obvious enrichment of B. This indicated that the low-temperature diffusion was conducive to the diffusion of B to the GBs. The proportion of serrated precipitates increased after the AD treatment, and the Mo-rich serrated precipitates contained B. Serrated precipitates have also occurred in austenitic stainless steels and nickel-based alloys [29–31]. In nickel-based alloys, the enrichment of B segregation was found at the serrated precipitates [32]. In Figures 3 and 7, the distribution of B and Ce in GB showed that Ce was more conducive to the discontinuous distribution of the precipitates. B was more inclined to inhibit the precipitates and drove the precipitates to appear as serrations. According to the results shown in Figures 2 and 3, the contents of Cr and Mo in the precipitates distributed at the straight GB were higher, while the content of Cr in the serrated precipitate was obviously lower than in the precipitates at straight GBs, and the content of Cr in the serrated precipitate was close to the matrix. In other words, there was no Cr-depleted zone at the interface of the serrated precipitate. The results shown in Figures 5 and 6 jointly verified that the interface of the serrated precipitate had a superior resistance to intergranular corrosion.

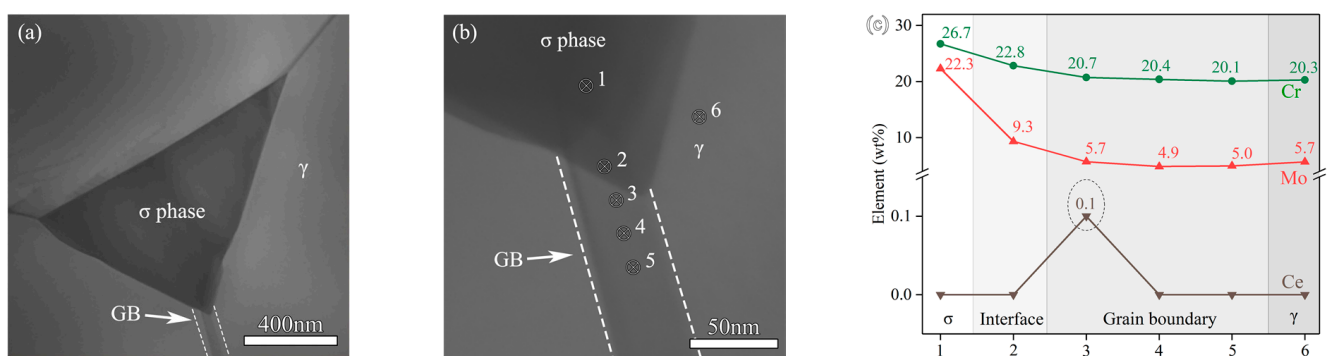


**Figure 7.** Aging at 950 °C for 1.5 h: (a,b) STEM, (c) distribution of elements in GBs.

Generally, due to the high Cr and Mo content of  $\sigma$ , it always led to a Cr-depleted zone near the precipitates and increased the intergranular corrosion of the S31254. There was no Cr-depleted zone at the interface of the Mo-rich serrated precipitate containing B [16,33,34].

As shown in Figure 8, after aging at 950 °C for 3 h and soaking in boiling  $\text{H}_2\text{SO}_4\text{-Fe}_2(\text{SO}_4)_3$ , there was a micropit on the surface at the junction of two types of precipitates. The intergranular corrosion was slight. According to the elemental distribution of the cross section, the corrosion of S31254–BCe in boiling  $\text{H}_2\text{SO}_4\text{-Fe}_2(\text{SO}_4)_3$  was mainly caused by the GB. However, the Mo-rich serrated precipitate was close to the surface due to the

uniform content of Cr around the serrated precipitates, so the depth of the intergranular corrosion attack was only 0.5  $\mu\text{m}$ . Another precipitate rich in both Cr and Mo was far from the surface. Therefore, there was no deep corrosion pit on the surface of section.

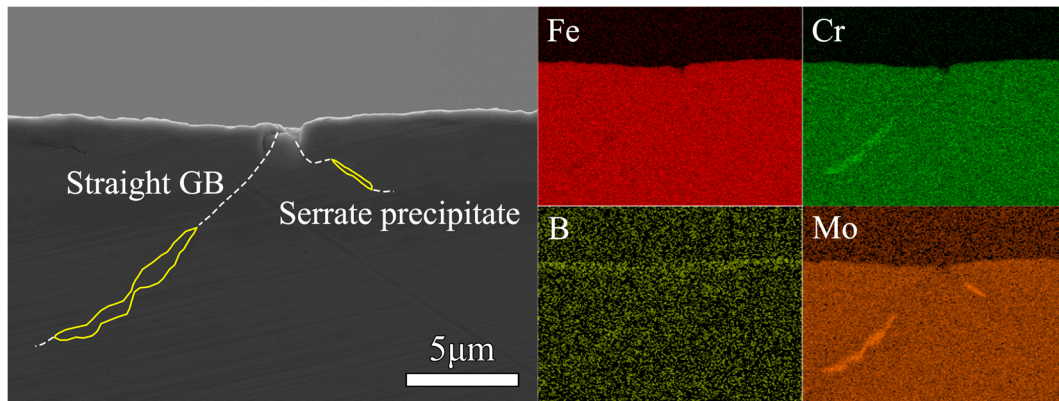


**Figure 8.** Section morphology and EDS of S31254–BCe sample aged for 3 h and soaked in boiling  $\text{H}_2\text{SO}_4\text{-Fe}_2(\text{SO}_4)_3$  for 24 h.

## 5. Conclusions

The precipitation of a Cr- and Mo-rich  $\sigma$  phase in SASSs seriously affects their thermoplasticity and corrosion resistance. In this study, B and Ce microalloying was used to reduce the segregation of Cr and Mo and inhibit the precipitates. A new air-cooling and low-temperature diffusion treatment method was adopted to further segregate more B and Ce elements at the GBs. Then, the samples were aged at 950  $^\circ\text{C}$ , and the influence of B and Ce on the precipitation behavior and corrosion resistance was studied. The main conclusions can be summarized as follows:

- (1) Air cooling and low-temperature diffusion prompted co-segregation of B, precipitate-forming elements, and Ce at the grain boundary (GB) at 950  $^\circ\text{C}$ . The heat-treatment process could inhibit the precipitation. Ce inhibited the nucleation of the precipitates. B induced the formation of Mo-rich precipitates, and the B-containing precipitates were serrated.
- (2) For aging at 950  $^\circ\text{C}$  within 3 h, the grain boundary segregation of B and Ce still had an obvious inhibitory effect on precipitates. The heat-treatment process could significantly suppress the segregation of Cr at the grain boundary and change the ratio of Mo and Cr elements in the precipitates. Compared with the traditional solution process, the number of precipitates was fewer and the distribution of precipitates was more intermittent.
- (3) The formation of B-containing serrated precipitates decreased the Cr-depleted zone near the grain boundary. This illustrated that the addition of B and Ce could lead to an extreme improvement in the corrosion resistance of S31254 SASSs.

**Author Contributions:** Methodology, Formal Analysis, Investigation, Writing—Original Draft, S.Y.; Resources, J.M., C.C., C.Z., J.R. and G.F.; Visualization, S.Y. and J.R.; Funding Acquisition, Z.J.; Conceptualization, Writing—Review and Editing, Funding Acquisition, P.H. All authors have read and agreed to the published version of the manuscript.

**Funding:** The present work was financially supported by the National Natural Science Foundation of China (Grant Nos. U1860204, 51871159, and 52204349).

**Data Availability Statement:** Not applicable.

**Conflicts of Interest:** The authors declare no conflict of interest.

## References

1. Zhang, S.C.; Li, H.B.; Jiang, Z.H.; Li, Z.X.; Wu, J.X.; Zhang, B.B.; Duan, F.; Feng, H.; Zhu, H.C. Influence of N on precipitation behavior, associated corrosion and mechanical properties of super austenitic stainless steel S32654. *J. Mater. Sci. Technol.* **2020**, *42*, 143–155. [[CrossRef](#)]
2. Koutsoukis, T.; RedjaMia, A.; Fourlaris, G. Characterization of precipitation sequences in super austenitic stainless steels. *Solid State Phenom.* **2011**, *172*, 493–498. [[CrossRef](#)]
3. Meguid, E.; Latif, A. Critical pitting temperature for type 254 SMO stainless steel in chloride solutions. *Corros. Sci.* **2007**, *49*, 263–275. [[CrossRef](#)]
4. Zhang, S.C.; Li, H.B.; Jiang, Z.H.; Feng, H.; Wen, Z.J.; Ren, J.Y.; Han, P.D. Unveiling the mechanism of yttrium significantly improving high-temperature oxidation resistance of super austenitic stainless steel S32654. *J. Mater. Sci. Technol.* **2022**, *115*, 103–114. [[CrossRef](#)]
5. Dou, Y.P.; Han, S.K.; Wang, L.W.; Wang, X. Characterization of the passive properties of 254SMO stainless steel in simulated desulfurized flue gas condensates by electrochemical analysis, XPS and TOF-SIMS. *Corros. Sci.* **2020**, *165*, 108405. [[CrossRef](#)]
6. Neville, A.; Hodgkiess, T. Study of passive film on stainless steels and high-grade nickel base alloy using X-ray photoelectron spectroscopy. *Br. Corros. J.* **2000**, *35*, 183–188. [[CrossRef](#)]
7. Wang, Q.; Wang, L.J.; Sun, Y.H.; Zhao, A.M. The influence of Ce micro-alloying on the precipitation of intermetallic sigma phase during solidification of super austenitic stainless steels. *J. Alloys Compd.* **2020**, *815*, 152418. [[CrossRef](#)]
8. Marin, R.; Hervé, C.; Zollinger, J.; Moukrane, D.; Lucile, L.R.  $\sigma$ -phase formation in super austenitic stainless steel during directional solidification and subsequent phase transformations. *Metall. Mater. Trans. A* **2020**, *51*, 3526–3534. [[CrossRef](#)]
9. Zhang, S.C.; Jiang, Z.H.; Li, H.B.; Zhang, B.B.; Fan, S.P.; Li, Z.X.; Feng, H.; Zhu, H.C. Precipitation behavior and phase transformation mechanism of super austenitic stainless steel S32654 during isothermal aging. *Mater. Charact.* **2018**, *137*, 244–255. [[CrossRef](#)]
10. Changmin, L.; Youngchai, L.; Changhee, L.; Hong, S. Precipitation behavior of the sigma phase with Ni and Mn content variations in superaustenitic stainless steel weld metal. *Mater. Charact.* **2018**, *144*, 148–154.
11. Chen, C.; Cheng, G.G. Delta-ferrite distribution in a continuous casting slab of Fe-Cr-Mn austenitic stainless steel. *Metall. Mater. Trans. B* **2017**, *48*, 2324–2333. [[CrossRef](#)]
12. Simcoe, C.R.; Elsea, A.R.; Manning, G.K. Study of the effect of boron on the decomposition of austenite. *JOM J. Miner. Met. Mater. Soc.* **1955**, *7*, 193–200. [[CrossRef](#)]
13. Ueno, M.; Inoue, T. Distribution of boron at austenite grain boundaries and bainitic transformation in low carbon steels. *Trans. Iron Steel Inst. Jpn.* **1973**, *13*, 210–217. [[CrossRef](#)]
14. Wang, T.H.; Wang, J.; Bai, J.G.; Wang, S.J.; Chen, C.; Han, P.D. Effect of boron on dissolution and repairing behavior of passive film on S31254 super austenitic stainless steel immersed in H<sub>2</sub>SO<sub>4</sub> solution. *J. Iron Steel Res. Int.* **2022**, *29*, 14. [[CrossRef](#)]
15. Li, S.; Ma, J.Y.; Wang, J.; Fan, G.W.; Li, H.B.; Jiang, Z.H.; Han, P.D.; Liang, W. Impact of boron addition on the hot deformation behavior and microstructure evolution of S31254. *Mater. Lett.* **2022**, *315*, 131971.1–131971.4. [[CrossRef](#)]
16. Zhang, Y.; Ma, J.Y.; Li, H.B.; Wang, H.X.; Du, Y.W.; Jiang, Z.H.; Han, P.D. Improved corrosion resistance of super austenitic stainless steel by B-induced nucleation of Laves phase. *Corros. Sci.* **2023**, *213*, 110974. [[CrossRef](#)]
17. Yu, J.T.; Zhang, S.C.; Li, H.B.; Jiang, Z.H.; Feng, H.; Xu, P.P.; Han, P.D. Influence mechanism of boron segregation on the microstructure evolution and hot ductility of super austenitic stainless steel S32654. *J. Mater. Sci. Technol.* **2022**, *112*, 184–194. [[CrossRef](#)]
18. Wang, X.F.; Chen, W.Q. Influence of cerium on hot workability of 00Cr25Ni7Mo4N super duplex stainless steel. *J. Rare Earths* **2010**, *2*, 295–300. [[CrossRef](#)]
19. Jeon, S.H.; Hur, D.H.; Kim, H.J.; Park, Y.S. Effect of Ce addition on the precipitation of deleterious phases and the associated intergranular corrosion resistance of 27Cr-7Ni hyper duplex stainless steels. *Corros. Sci. J. Environ. Degrad. Mater. Its Control* **2015**, *90*, 313–322. [[CrossRef](#)]
20. Zhang, S.C.; Yu, J.T.; Li, H.B.; Jiang, Z.H.; Geng, Y.F.; Feng, H.; Zhang, B.B.; Zhu, H.C. Refinement mechanism of cerium addition on solidification structure and sigma phase of super austenitic stainless steel S32654. *J. Mater. Sci. Technol.* **2022**, *102*, 105–114. [[CrossRef](#)]
21. Faulkner, R.G. Combined grain boundary equilibrium and non-equilibrium segregation in ferritic/martensitic steels. *Acta Metall.* **1987**, *35*, 2905–2914. [[CrossRef](#)]
22. He, X.L.; Chu, Y.Y.; Jonas, J.J. Grain boundary segregation of boron during continuous cooling. *Acta Metall.* **1989**, *37*, 147–161. [[CrossRef](#)]
23. Genichi, S.; Taishi, F.; Takuya, H. Grain boundary segregation behavior of boron in low-alloy steel. *Metall. Mater. Trans. A Phys. Metall. Mater. Sci.* **2014**, *45*, 1876–1882.
24. Zhang, X.L.; Xun, M.N.; Ma, J.Y.; Liang, X.H.; Zhang, C.L.; Li, H.B.; Jiang, Z.H.; Fan, G.W.; Han, P.D. Effects of heat treatment on precipitation and corrosion resistance of cerium-containing super austenitic stainless steel S31254. *Corros. Commun.* **2022**, *8*, 1–8. [[CrossRef](#)]
25. Lee, J.S.; Fushimi, K.; Nakanishi, T.; Hasegawa, Y.; Park, Y.S. Corrosion behavior of ferrite and austenite phases on super duplex stainless steel in a modified green-death solution. *Corros. Sci.* **2014**, *89*, 111–117. [[CrossRef](#)]

26. Xin, J.J.; Song, Y.T.; Fang, C.; Wei, J.; Huang, C.J.; Wang, S.X. Evaluation of inter-granular corrosion susceptibility in 316LN austenitic stainless steel weldments. *Fusion Eng. Des.* **2018**, *133*, 70–76. [[CrossRef](#)]
27. Wang, J.; Cui, Y.S.; Bai, J.; Dong, N.; Liu, Y.; Zhang, C.L.; Han, P.D. The mechanism on the B addition to regulate phase precipitation and improve intergranular corrosion resistance in UNS S31254 super austenitic stainless steels. *J. Electrochem. Soc.* **2019**, *166*, C600–C608. [[CrossRef](#)]
28. Qurashi, M.S.; Cui, Y.S.; Wang, J.; Dong, N.; Han, P.D. Erosion and passivation of borated 254 SMO stainless steel in simulated flue gas desulfurization solution. *Int. J. Electrochem. Sci.* **2020**, *15*, 2987–3002. [[CrossRef](#)]
29. Hong, S.M.; Min, D.J.; Fleur, E. Effect of grain boundary serration on the tensile properties of the super 304H heat resistant austenitic stainless steel. *Mater. Sci. Forum* **2010**, *654*, 170–173. [[CrossRef](#)]
30. Kim, K.J. Investigation on the formation of serrated grain boundaries with grain boundary characteristics in an AISI 316 stainless steel. *J. Nucl. Mater.* **2009**, *393*, 249–253. [[CrossRef](#)]
31. Hong, H.U.; Kim, I.S.; Choi, B.G.; Kim, M.Y.; Jo, C.Y. The effect of grain boundary serration on creep resistance in a wrought nickel-based superalloy. *Mater. Sci. Eng. A* **2009**, *517*, 125–131. [[CrossRef](#)]
32. Letellier, L.; Chambrelaud, S.; Duval, P.; Blavette, D. Grain boundary segregation in nickel base superalloys Astroloy: An atom-probe study. *Appl. Surf. Sci.* **1993**, *67*, 305–310. [[CrossRef](#)]
33. Wang, J.; Cui, Y.S.; Bai, J.G.; Dong, N.; Liu, Y.; Zhang, C.L.; Han, P.D. Effect of B addition on the microstructure and corrosion resistance of S31254 super austenitic stainless steels after solid solution treatment. *Mater. Lett.* **2019**, *252*, 60–63. [[CrossRef](#)]
34. Zhang, S.C.; Li, H.B.; Jiang, Z.H.; Zhang, B.B.; Li, Z.X.; Wu, J.X.; Fan, S.P.; Feng, H.; Zhu, H.C. Effects of Cr and Mo on precipitation behavior and associated intergranular corrosion susceptibility of super austenitic stainless steel S32654. *Mater. Charact.* **2019**, *152*, 141–150. [[CrossRef](#)]

**Disclaimer/Publisher’s Note:** The statements, opinions and data contained in all publications are solely those of the individual author(s) and contributor(s) and not of MDPI and/or the editor(s). MDPI and/or the editor(s) disclaim responsibility for any injury to people or property resulting from any ideas, methods, instructions or products referred to in the content.